

Article

Numerical Investigation of Combustion Mechanism with Multi-Position Injection in a Dual-Mode Combustor

Wenxiong Xi ¹, Hui Xu ¹, Tianyang Dong ², Zhiyong Lin ² and Jian Liu ^{1,*} 

¹ Research Institute of Aerospace Technology, Central South University, Changsha 410012, China; 13739076081@163.com (W.X.); xuhui021108@163.com (H.X.)

² School of Aeronautics and Astronautics, Sun Yat-Sen University, Guangzhou 510006, China; dongty5@mail2.sysu.edu.cn (T.D.); linzhiyong@mail.sysu.edu.cn (Z.L.)

* Correspondence: jian.liu@csu.edu.cn

Abstract: To improve the flame propagation, combustion stability, and uniformity of the temperature field, multi-position injection is applied in a dual-mode combustor by controlling heat release in different locations. Using the chemical reaction of the finite rate combustion model and the detailed reaction mechanism of hydrogen combustion as described by Jachimowski, the influence of different multi-position injection patterns in a dual-mode combustor is analyzed. The one-equation Large Eddy Simulation (LES) turbulence model was chosen to define the sublattice turbulent viscous terms in a three-dimensional scramjet model. Based on a combustion chamber, the effect of the injection equivalent ratio (0.35–0.70), the relative position of the nozzle holes, and the injection pressure on the combustion process and flow field characteristics are analyzed with multi-position injection. The combustion efficiency, total pressure recovery coefficients, and pressure distribution under different operation conditions are compared. We observed that the combustion intensity increases and the upstream combustion shock string distance becomes greater with increased equivalent ratios. When the global equivalent ratio of multi-position injection remains unchanged, the arrangement of nozzles with the small injection spacing, i.e., two injection holes arranged face to face on the upper and lower walls, or the setting of multiple injection holes with the same pressure, can effectively increase the stability rate of the combustion flow field. In addition, the combustion efficiency at the outlet and the internal pressure of the combustion chamber in the stable state are also improved, relative to the increased total pressure loss.

Keywords: combustion mechanism; multi-position injection; equivalent ratios; relative position



Citation: Xi, W.; Xu, H.; Dong, T.; Lin, Z.; Liu, J. Numerical Investigation of Combustion Mechanism with Multi-Position Injection in a Dual-Mode Combustor. *Aerospace* **2023**, *10*, 656. <https://doi.org/10.3390/aerospace10070656>

Academic Editor: Sergey Leonov

Received: 25 May 2023

Revised: 20 July 2023

Accepted: 20 July 2023

Published: 24 July 2023



Copyright: © 2023 by the authors. Licensee MDPI, Basel, Switzerland. This article is an open access article distributed under the terms and conditions of the Creative Commons Attribution (CC BY) license (<https://creativecommons.org/licenses/by/4.0/>).

1. Introduction

With its wide range of cruising speeds and high specific impulse, the scramjet engine is currently considered the best choice for achieving hypersonic flight within the atmosphere. When a scramjet engine operates normally, due to the extremely fast inflow of air into the engine, the time for fuel injection, mixing, and combustion in the combustion chamber is only about 1 ms [1], which makes it difficult to maintain a stable flame. The Central Institute of Aviation Motors (CIAM) was the first to use a cavity structure to test a dual-mode hydrogen-fueled scramjet engine jointly developed by Russia and France [2]. Subsequently, many scholars have confirmed the significant role of the cavity structure in stabilizing the flame in the scramjet combustion chamber based on extensive experiments [3–5]. Currently, the cavity flame-holding structure has become one of the most common flame stabilization structures in scramjet combustion chambers. In addition to the cavity, baffles and rear steps are also commonly used flame stabilization structures in scramjet combustion chambers [6,7].

During actual operation, the existence of an isolator is a prerequisite for the stable operation of a dual-mode combustion chamber, as it plays an extremely important role in the

mode transition of a dual-mode engine, as shown in Figure 1. Penzin [8] research supersonic isolators and proposed two working modes, i.e., separated shock waves and pseudo-shock waves. He suggested that the pseudo-shock wave mode with a pre-combustion shock train in the flow channel was the ideal working mode of the isolator. When the engine is working, the fuel starts a chemical reaction after injection, and the heat from combustion causes a sudden increase in the pressure inside the combustion chamber [9], which is significantly higher than the pressure in the intake. A large enough pressure difference causes a pre-combustion shock wave to appear in front of the combustion chamber; this shock wave then interacts with the separated boundary layer to form a pre-combustion shock train [10]. The pre-combustion shock train can decelerate the supersonic flow from the intake to the airflow speed required by the combustion chamber. Through the shock train, the low-pressure airflow at the intake can achieve a sufficient increase in pressure to match the high back pressure of the downstream combustion chamber. The deceleration of the airflow brought about by the shock train increases the static temperature of the airflow. With the increase in pressure, ignition delay is reduced, and ignition time is shortened. At the same time, the decreased flow velocity increases the residence time of the airflow, which helps stabilize the combustion flame [11]. When the back pressure of the combustion chamber increases, the length of the pre-combustion shock train increases and the leading edge moves upstream. Studies have shown that this forward development of the shock train position is very rapid, i.e., it can range from a few milliseconds to tens of milliseconds [12]. If it moves forward to the inlet of the isolator, the shock train will be very sensitive to pressure changes. At this time, even a small increase in back pressure pushes the shock train out of the isolator and into the intake [13]. When the leading edge of the shock train is close to the intake, it may cause a loss of the captured flow, an increase in pressure, thermal load, and drag, and a decrease in thrust; any further advancement may lead to the intake not starting [8].

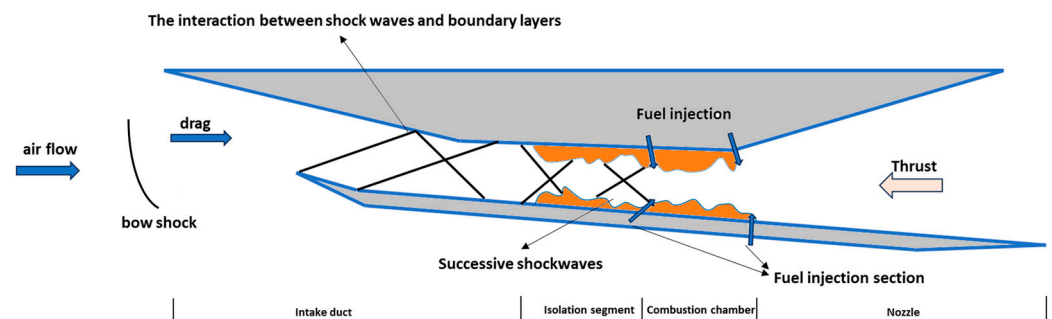


Figure 1. Schematic of a scramjet engine.

The Planar Laser-Induced Fluorescence (PLIF) technique is often used in experiments to mark the location of flames, enabling visualization of the flame structure in the research of scramjet combustion chambers. Ben-Yakar et al. [14] and Johansen et al. [15] used OH-PLIF images as markers to identify the location of combustion flames and conducted experimental research on the distribution of the hydrogen fuel jet in a scramjet combustion chamber. It was found that the main diffused fuel stream and the contact position with the incoming air stream formed an arc-shaped reaction zone, while a recirculation zone was generated upstream of the injection hole. By moving the optical system and using two independent camera views, imaging was performed over the entire optically accessible range of the combustion chamber. The results showed the development of a highly turbulent flame structure and provided an experimental database for numerical model evaluation. Carter et al. [16] conducted experimental research using laser and optical fluorescence detection equipment and observed premixed turbulent flames using CH-PLIF technology. Those authors showed that good CH-PLIF signal-to-noise and signal-to-background ratios were attained at a 10 kHz interrogation rate and that the spatial resolution (of the CH layer) was reasonably good as well. Cantu et al. [17] used CH-PLIF technology to study ethylene

premixed flames in bimodal cavity combustion chambers and compared the measurement results with Large Eddy Simulation and Reynolds-averaged numerical simulation results. The comparison revealed that the dominant effect of flame propagation was freestream turbulence rather than heat release and concentration gradients. Moura et al. [18] utilized planar laser-induced fluorescence (PLIF) of OH radicals to probe the combustion process. Supplementary Large Eddy Simulation under experimental conditions revealed that the combustion process in the supersonic scramjet engine is multimodal, with neither premixed nor non-premixed combustion dominating, but rather, with each contributing significantly to heat release. These modes coexist within the engine. For both modes, combustion was confirmed to occur in multiple combustion regimes. Their work provides new insights into supersonic turbulent combustion processes and enhances our understanding of this technology.

To further improve the specific impulse performance of the hydrogen-fueled scramjet engine, the combustion mode and operating route of a hydrogen-fueled scramjet engine are analyzed [19]. The one-dimensional method was used for the numerical simulation of a two-stage hydrogen jet scramjet engine at a Mach number ranging from 4–7. Choubey et al. [20] presented the current status of the development of hydrogen-fueled scramjet engines and the challenges faced when using hydrogen fuels. In addition, the advantages of using hydrogen as a fuel compared to other hydrocarbon fuels were thoroughly discussed. Choubey [21] analyzed some mixture enhancement methods based on cavity-based injection, as proposed in recent research works. The impact of the cavity on the performance of the scramjet engine combustion chamber was reviewed from three aspects: changes in the shape/geometric structure of the cavity flame holder, the location of the fuel/air injection scheme, and the latest progress in the development of the resonant cavity.

Kannaiyan [22] conducted a study on the combustion of ethylene fuel under single-step and multi-step reactions based on the heat release rate parameters at different locations in the combustion chamber. He et al. [23] conducted experimental and numerical studies on the flame stability characteristics of ethylene fuel in a scramjet concave cavity combustor. The results show that a shorter injection distance can effectively reduce the lean purge limit of the combustion chamber, while the rear wall expansion chamber and a longer injection distance can effectively increase the rich blowout limit. Ma et al. [24] used a mixture of hydrogen/methane and hydrogen/ethylene fuels in a strut combustion chamber and tracked the combustion flame with OH distribution. They found that the blending injection of hydrogen with hydrocarbon fuels led to a decrease in flame combustion intensity and combustion efficiency. Zhao et al. [25] used HO_2 as a marker for the self-ignition process in hydrogen combustion and performed Large Eddy Simulations on the combustion mechanism of optimal frequency pulsed sonic jets. They found that pulsating jets can enhance the heat release rate of the non-premixed zone while having little effect on the heat release of premixed combustion.

To date, many experimental and numerical simulation studies have been carried out on the structures, injection position, and equivalence ratio of the stable flame structure of scramjet chambers. To enhance flame propagation, combustion stability, and the uniformity of the temperature field, in this study, a multi-position injection strategy is implemented in a dual-mode combustor by controlling heat release at various locations. By utilizing the chemical reaction source of the finite rate combustion model and Jachimowski's detailed hydrogen combustion reaction mechanism, we could analyze the impact of different multi-position injection patterns in a dual-mode combustor. A one-equation Large Eddy Simulation (LES) turbulence model was selected to close the subgrid-scale turbulent viscous terms in a three-dimensional scramjet model. The effects of various injection equivalent ratios (0.35–0.70), nozzle hole positions, and injection pressure on the combustion process and flow field characteristics were analyzed based on the combustion chamber with multi-position injection. Furthermore, the relationships between the influences by different injection holes with multi-position injection are discussed.

2. Numerical Methods

2.1. Computational Domain and Related Parameters

The configuration of the scramjet combustion chamber [26] used for the calculations in this study is shown in Figure 2. The length of the combustion chamber (L) is 700 mm and the inlet height (H) is 50 mm. The combustion chamber adopts a design that expands the lower wall surface of the cavity, and the inclination angle (θ) of the cavity is 2° . The arrangement of the combustion chamber nozzle refers to the classical test model with a total width of the combustion chamber of 70 mm. To simplify, a single nozzle is selected and the calculated width of the combustion chamber in the spanwise direction is set as 10 mm. Two side walls are set as symmetrical to reduce the effects of the simplified model. On the upper wall of the combustion chamber, hydrogen injection holes U1 and U2 are arranged, and injection holes D1, D2, and D3 are arranged on the lower wall. The diameter of the injection holes is 1 mm, and ejection occurs perpendicular to the wall. The centers of upper wall injection holes U1 and U2 are respectively 220 mm and 300 mm from the combustion chamber inlet. Injection hole D1 is arranged on the upstream wall of the cavity and Injection hole D2 is arranged inside the cavity. Injection holes D1 and D2 are arranged on the two sides of the front wall of the cavity at a distance of 15 mm from each other. Nozzle D3 is arranged on the downstream wall of the cavity, and its center is 15 mm from the rear edge of the cavity. The distance from the cavity to the combustion chamber entrance (ΔL) is 180 mm. The total length of the cavity (l) is 70 mm with a height (h) of 10 mm, an aspect ratio (l/d) of 7, and an angle of the rear wall (γ) of 30° .

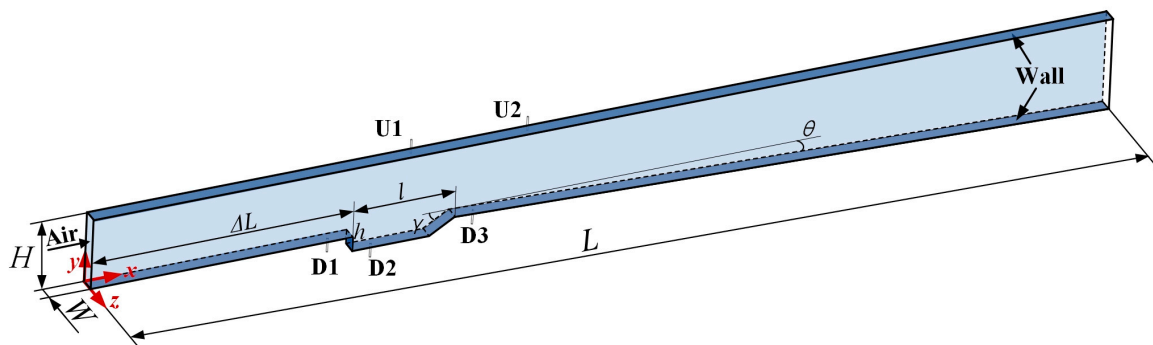


Figure 2. Schematic of the computational domain of the combustion chamber.

To conduct research on multi-position injection flame development and the combustion flow field in a scramjet engine [27], the specific calculation cases and corresponding parameters are shown in Table 1. In the table, Cases 1, 2, and 3 are used to study the effects of the injection equivalence ratios on the flame distribution and flow structures of the combustion chamber; Cases 1, 4, and 5 are used to study the effects of the relative positions of the injection holes (same side injection, two-side injection, and far distance two-side injection, respectively); Cases 1, 6, and 7 are used to study the effects of the injection pressure (high pressure in the front injection hole and low pressure in the back injection hole, low pressure in the front injection hole and high pressure in the rear injection hole, and the same pressure in the front and rear injection holes).

Table 1. Parameters for the different cases.

Case	Injection Pressure Setting/MPa	Global Equivalent Ratio	Nozzle Location
1	2.0	0.35	U2, D1
2	2.0	0.52	U1, D1, D3
3	2.0	0.70	U1, U2, D1, D3
4	2.0	0.35	D3, D1
5	2.0	0.35	U1, D1
6	$P_{U2} = 3.0, P_{D1} = 1.0$	0.35	U2, D1
7	$P_{U2} = 1.0, P_{D1} = 3.0$	0.35	U2, D1

2.2. Calculation Method and Boundary Condition

The turbulence model adopts a one-equation Large Eddy Simulation (LES) turbulence model to determine the subgrid-scale turbulence viscosity terms [28]. The Leonard stress, subgrid-scale Reynolds stress, and cross-stress are modeled using the linear Boussinesq relationship.

The transport equation is solved according to the usual inlet and solid surface boundary conditions of turbulent kinetic energy. The continuity equation, momentum equation, and energy equation are discretized using the second-order upwind scheme. Spatial discretization is performed using a second-order scheme with a Total Variation Diminishing (TVD) limiter applied for improved computational convergence. The Roe-Flux Difference Splitting (FDS) method is used for the decomposition of physical fluxes, and the time term is discretized using the second-order implicit scheme. The numerical simulation neglects the effects of heat conduction and flow diffusion. The chemical reaction source is modeled using a finite-rate combustion model with walls treated as no-slip adiabatic surfaces. The combustion chemistry is based on the detailed Jachimowski mechanism [29] for hydrogen, with eight components and nineteen reaction steps, as specifically shown in Table 2.

Table 2. Parameters of hydrogen ($O_2 + 3.76 N_2$) combustion mechanism with eight components and nineteen reaction steps.

Number	Reaction	A ($mole \cdot cm \cdot s \cdot k$)	n	E ($cal \cdot mole^{-1}$)
1	$H_2 + O_2 = HO_2 + H$	1.00×10^{14}	0.00	56,034.7
2	$H_2 + O_2 = OH + O$	2.60×10^{14}	0.00	16,810.4
3	$H_2 + O = OH + H$	1.80×10^{10}	1.00	8905.5
4	$H_2 + OH = H + H_2O$	2.20×10^{13}	0.00	5153.2
5	$OH + OH = O + H_2O$	6.30×10^{12}	0.00	1090.7
6	$H + OH + M = H_2O + M$	2.20×10^{22}	2.00	0.0
			$H_2O/6.0$	
7	$H + H + M = H_2 + M$	6.40×10^{17}	1.00	0.0
			$H_2/2.0/H_2O/6.0$	
8	$H + O + M = OH + M$	6.00×10^{16}	0.60	0.0
			$H_2O/5.0$	
9	$H + O_2 + M = HO_2 + M$	2.10×10^{15}	0.00	−1000.6
			$H_2/2.0/H_2O/16.0$	
10	$O + O + M = O_2 + M$	6.00×10^{13}	0.00	−1801.1
11	$HO_2 + H = OH + OH$	1.40×10^{14}	0.00	1080.7
12	$HO_2 + H = H_2O + O$	1.00×10^{13}	0.00	1080.7
13	$HO_2 + O = O_2 + OH$	1.50×10^{13}	0.00	950.6
14	$HO_2 + OH = H_2O + O_2$	8.00×10^{12}	0.00	0.0
15	$HO_2 + HO_2 = H_2O_2 + O_2$	2.00×10^{12}	0.00	0.0
16	$H + H_2O_2 = H_2 + H_2O$	1.40×10^{12}	0.00	3602.2
17	$O + H_2O_2 = OH + HO_2$	1.40×10^{13}	0.00	6404.0
18	$H_2O_2 + OH = H_2O + HO_2$	6.10×10^{12}	0.00	1430.9
19	$H_2O_2 + M = OH + OH + M$	1.20×10^{17}	0.00	45,528.2
			$H_2O/15.0$	

The simulated scramjet engine operates at a flight Mach number of 6 [30]. The incoming flow Mach number at the combustion chamber is 3.0, with a total pressure of $P_0 = 2.11$ MPa, a total temperature of $T_0 = 1650$ K, and a static temperature of $T = 702$ K. Hydrogen fuel is ejected perpendicular to the wall with a total temperature of $T_t = 300$ K, and combustion is carried out through self-ignition. The computational model employs symmetric boundary conditions on both sides with no-slip wall conditions on the upper and lower surfaces. The five fuel injection holes are set with a pressure inlet boundary condition. Combustion calculations were carried out after ensuring that the cold flow field computation had reached dynamic stability.

Engine performance is mainly judged by the oxygen consumption rate, total pressure recovery coefficient, and combustion efficiency. The calculation formula for the oxygen consumption rate, total pressure recovery coefficient, and combustion efficiency are listed below.

The formula for oxygen consumption rate:

$$\phi = \frac{q_m(O_2)_{in} - \int_{A_{out}} \rho \omega(O_2) u dA_{out}}{q_m(O_2)_{in}} \quad (1)$$

The formula for total pressure recovery factor:

$$\sigma = \frac{\sum_{i=1}^n A_i p_{0,out,i}}{\sum_{i=1}^n A_i} \cdot \left(\frac{\sum_{i=1}^m A_i p_{0,in,i}}{\sum_{i=1}^m A_i} \right)^{-1} \quad (2)$$

The formula for combustion efficiency:

$$\phi = \frac{q_m(H_2)_{in} - \int_{A_{out}} \rho \omega(H_2) u dA_{out}}{q_m(H_2)_{in}} \quad (3)$$

where $q_m(O_2)_{in}$ is the mass flow rate of oxygen at the inlet of the combustion chamber, $q_m(H_2)_{in}$ is the total mass flow rate of hydrogen injection into the combustion chamber, A_{out} is the outlet area of the combustion chamber, $\sum_{i=1}^n A_i p_{0,out,i} / \sum_{i=1}^n A_i$ is the area-weighted averaged outlet pressure, and $\sum_{i=1}^m A_i p_{0,in,i} / \sum_{i=1}^m A_i$ is the area-weighted averaged inlet pressure.

2.3. Mesh Details

This section mainly introduces the grid generation of the model. As the combustion chamber is relatively long, a coarser grid is employed for conducting numerical calculations of flow field changes throughout the afterburning combustion chamber. Figure 3a provides an overview of the grids of the combustion chamber. As the injection holes in the combustion chamber are distributed on both the upper and lower surfaces, grid refinement was applied in the upper and lower sections of the combustion chamber and inside the cavity. In addition, grid refinement was performed on the upper and lower surfaces of the combustion chamber to enhance the accuracy of the boundary layer calculations. Figure 3b presents the grid details near the injection holes, where the O-block method was used for grid refinement, with a grid size of 0.02 mm. The total grid number of the computational domain is 4 million, with a minimum grid size of 0.1 mm and a maximum grid size of 0.25 mm.

For the grid validation employed in the investigation of the combustion characteristics in the combustor, three sets of grids with different scales were utilized: coarse (approximately 2.5 million cells), medium (approximately 4 million cells), and fine (approximately 5.5 million cells). Figure 3c illustrates the impact of these three grid sizes on the pressure distribution along the upper wall of the supersonic combustion chamber. It can be observed that the coarse grid exhibits significant differences in terms of the pressure of the rear cavity shock of the combustion chamber compared to the medium and fine grids. On the other hand, the medium and fine grids show a good overall fit. Considering both computational accuracy and limitations in computational resources, this study adopted the medium-scale combustion chamber grid for the numerical investigation of the combustion characteristics in a multi-injection scramjet combustion chamber.

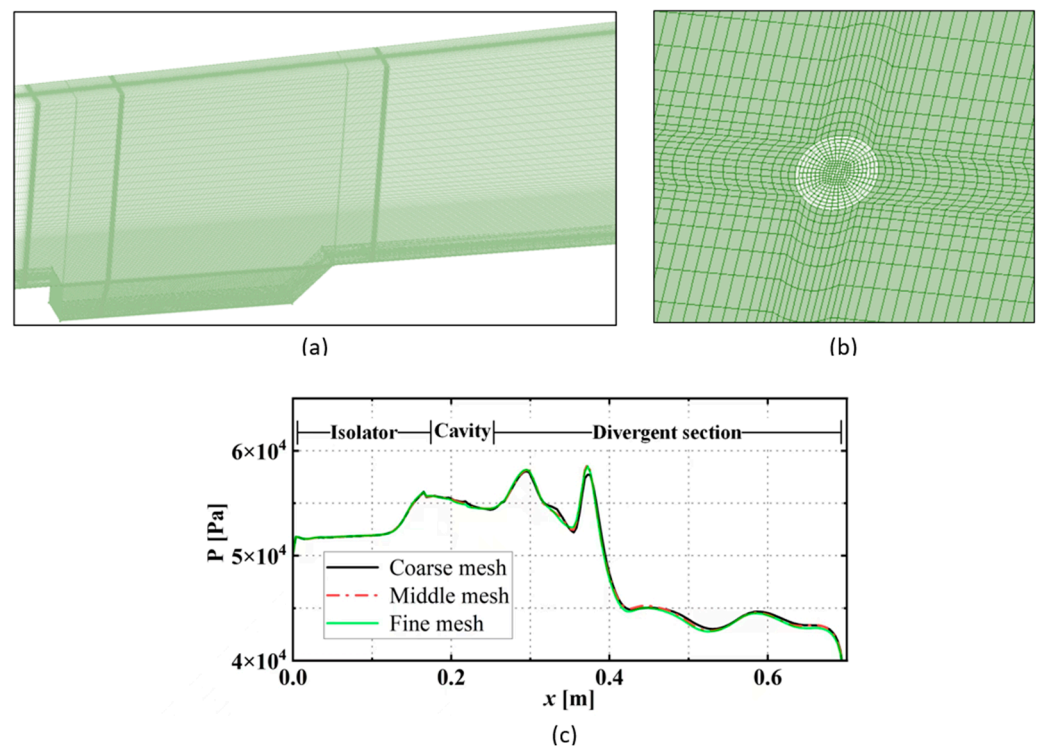


Figure 3. Mesh details in the computational domain. (a): the combustion chamber; (b): the injection hole; (c): Grid independence study.

2.4. Model Verification

This study uses the strut-based scramjet engine from the German Aerospace Center for the model validation shown in Figure 4a. This model has comprehensive experimental results for method validation. Additionally, the model uses hydrogen as the injection fuel and the inlet size of the combustion chamber is similar to that of the model used in this work. The validation model was built with a grid number of about 2 million, and the experimental results were obtained from Franklin et al. [31]. A comparison between the calculated and experimental values of the pressure distribution on the lower surface of the combustion chamber, under cold flow conditions and with fuel injection through the strut tail, is shown in Figure 4b. Generally speaking, the trend of pressure changes in the streamwise direction (x) is essentially the same, with some relatively large errors at several extreme regions, i.e., where high-pressure shockwaves formed due to the high-speed inflow acting on the strut, being reflected on the lower surface of the combustion chamber.

Under the condition of unburned flow, the hydrogen flow rate is fast and there is no high-temperature heat source to support it, so it is difficult for the hydrogen emitted from the tail of the straight plate to effect large-area mixed combustion; as such, ignition is needed. Figure 4c,d respectively show comparisons of the calculated time-averaged velocity and the time-averaged temperature distributions along the spanwise direction (y) with the experimental results after hydrogen ignition at $x = 125$ mm. The calculated values of the time-averaged velocity and the time-averaged temperature distributions at different locations agree with the experimental results. In general, the results obtained by this numerical method are consistent with the distribution trend of the experimental results, which indicates that the adopted numerical method is reasonable.

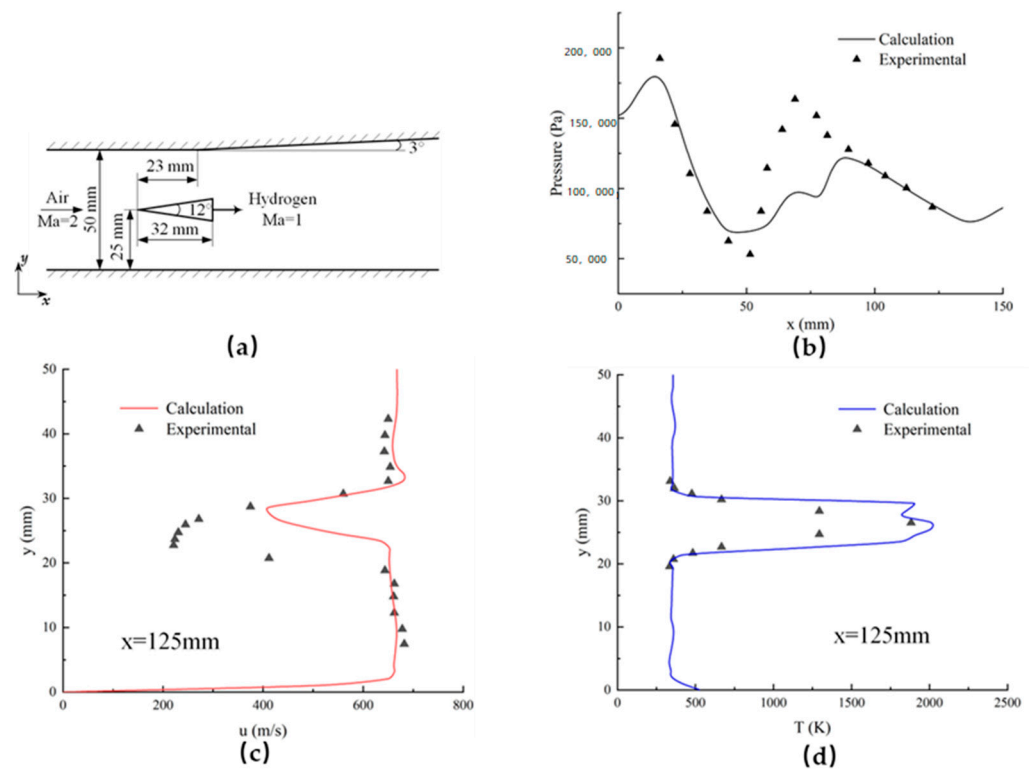


Figure 4. (a) Schematic of the DLR combustion chamber; (b) Comparison of the pressure distribution on the lower wall under unburned condition; (c) Comparison of the velocity distribution along the y direction; (d) Comparison of temperature distribution along the y direction.

3. Results and Discussion

3.1. Effects of the Equivalent Ratio

Figure 5 shows changes in the mass fraction of OH free radicals inside the combustion chamber over time for Case 1. According to the mechanism of the H_2 chemical reaction kinetics, OH is used to indicate the exothermic region of combustion and HO_2 is used as a pre-indicator for the autoignition process. Through fine simulation of the flame structure, it may be concluded that during autoignition, HO_2 appears before OH. For Case 1, injection holes U2 and D1 are opened and the distribution and intensity of the OH indicate the structure and status of the flames inside the combustion chamber. From the figure, the fuel injection time is short and the combustion intensity in the combustion chamber is weak at $t = 1.8$ ms. The OH on the upper wall of the combustion chamber mainly appears in the plume-like downstream region of the U2 injection hole and in a small triangular recirculation region upstream of the injection hole formed by bow shocks. Meanwhile, OH mainly appears on the lower wall of the combustion chamber inside and downstream of the cavity. At this time, due to weak combustion, there is no strong separation of the boundary layer, and fuel combustion mainly occurs inside and downstream of the cavity.

At $t = 3.0$ ms, the heat release intensity of the fuel reaction gradually increases with the continuous increase in the fuel mass flow injected into the combustion chamber. Due to the high temperature and high pressure produced by fuel combustion interacting with the incoming air flow, the reaction zone leads to the upstream propagation of combustion shockwaves. This also causes further separation of the boundary layer at the cavity position. It can be seen from the figure that the OH formed by the combustion of the fuel injected by D1 gradually diffuses from the inside of the cavity to the main stream. The fuel injected from the upper wall is pushed by the advancing combustion shockwaves, causing boundary layer separation at a distant upstream position from the U2 injection hole and forming a large region of slow recirculation. This facilitates the combustion of fuel injected from the U2 injection hole in the upstream recirculation zone, which is shown in the figure as the

formation of a certain region of OH free radicals upstream of the U2 injection hole. As the fuel injected from the lower wall continues, the reaction zone inside the cavity extends into the main stream. At $t = 5.2$ ms, the air flow channel deflects toward the upper wall, and the recirculation zone upstream of the U2 port detaches due to the expansion of combustion heat products in the cavity and the main stream. Therefore, no OH free radicals form upstream of U2, and the reaction zone of the fuel on the upper wall is mainly in the wake region of the fuel injected from U2. At this time, the state of fuel combustion is basically stable. At $t = 8.0$ ms, it is observed that the main fuel combustion on the lower wall of the combustion chamber in Case 1 occurs inside the cavity, extending to a certain depth inside the main stream and spreading downstream with the incoming air flow.

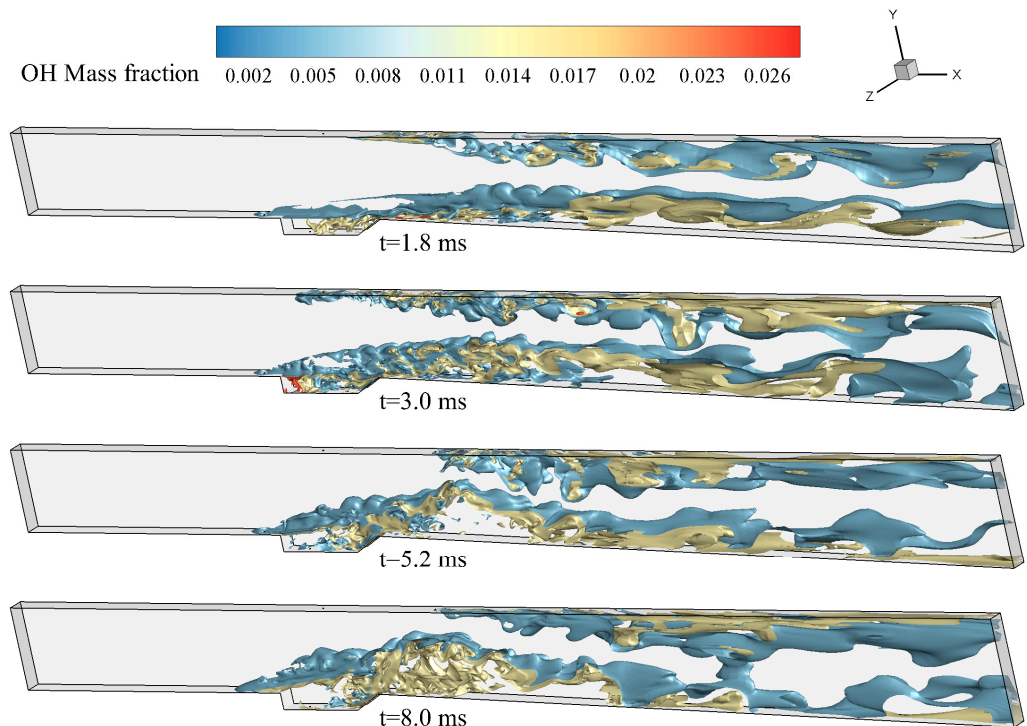


Figure 5. Mass fraction distributions of OH free radicals inside the combustion chamber for Case 1, varied with time.

Figure 6a displays the distributions of the combustion chamber pressure at $t = 8$ ms for Cases 1–3. As shown in the figure, the combustion shock wave chain formed inside the combustion chamber of Case 1 has progressed a shorter distance upstream, and the shock wave chain finally stabilizes at a position not far upstream of the D1 injection hole. Compared to the dual injection holes in the Case1 combustion chamber, Case 2 features three injection holes (U1, D1, and D3) with the same injection pressure and a global equivalence ratio of the injection which is higher than that of Case 1. It can be found that the change in the combustion region inside the combustion chamber of Case 2 is basically the same as that of Case 1, and the method of steady combustion is also basically consistent. The combustion of fuel on the upper wall of the combustion chamber mainly occurs downstream of the wake region. In Case 2, the intensity of the combustion shock wave chain is higher and the upstream extension into the combustion chamber is longer than in Case 1 due to the higher injection equivalence ratio. Observing the pressure distribution in the Case 3 combustion chamber, its internal pressure is the highest and the distance from upstream of the combustion shock wave chain is the greatest of the three cases. In the middle of the combustion chamber, several high-pressure regions can be seen, which are formed by multiple reflections of the combustion shock wave due to the large separation of the boundary layer.

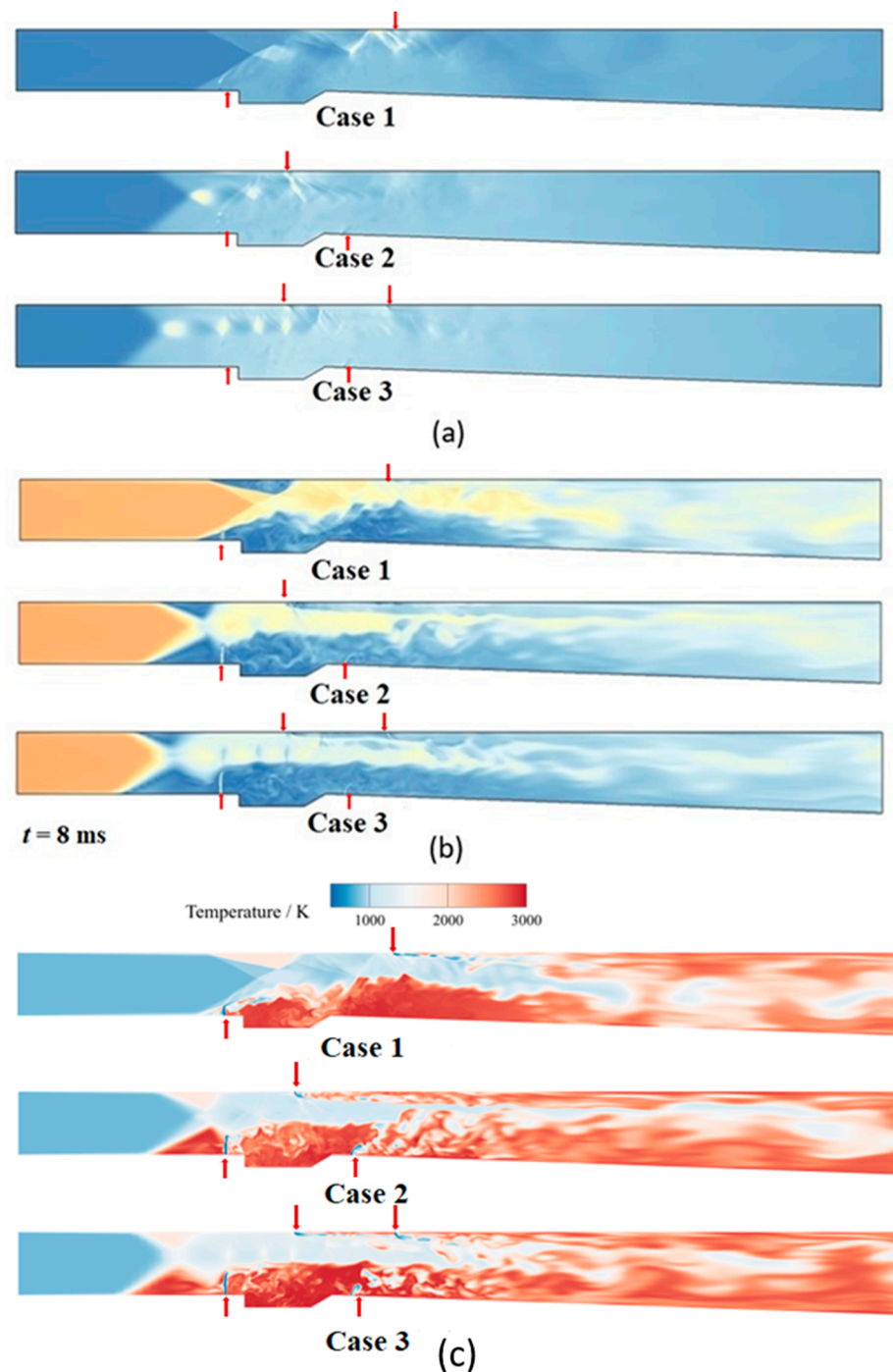


Figure 6. (a) Pressure distributions of the combustion chamber for Cases 1, 2, and 3; (b) Mach number distributions of the combustion chamber for Cases 1, 2, and 3. (c) Temperature distributions of the combustion chamber for Cases 1, 2, and 3.

Figure 6b shows the Mach number distributions inside the combustion chambers for Cases 1–3. As shown in the figure, the air flow channel clings to the upper wall of the combustion chamber for Case 1. In the case of multi-position injection, two bow-shaped shock waves form upstream of the two injection holes, and the interaction with the combustion shock wave chain formed by the fuel combustion causes a large region of narrowing in the air passage, i.e., the boundary layer separation on the upper and lower walls is larger, which is beneficial for the mixing and combustion of the fuel. Therefore, multi-position injection is more conducive to the mixing and burning of fuel in a scramjet

engine. The combustion shock wave chain in Case 2 ultimately stabilizes at a middle position upstream of the D1 injection hole. In addition, due to the forward movement of the combustion shockwave chain, the boundary layer separation regions on both sides of the upper and lower walls of the combustion chamber also move upstream. In Case 3, the air channel is compressed to a narrow width and the incoming air Mach number in the air channel gradually decreases with flow development. Figure 6c presents the temperature distributions inside the combustion chambers for Cases 1–3. In contrast with the data in Figure 6b, the temperature distributions are inverse to the Mach number distributions for all cases. It is shown that the heat release from the combustion is concentrated in regions with low velocity, such as the cavity.

Comparisons of the combustion efficiency at the outlet of the combustion chamber varying with time for Cases 1, 2, and 3 are shown in Figure 7a. The calculation formula for combustion efficiency can be seen in Equation (3). As shown in the figure, the time required for the flow field of the Case 1 combustion chamber to stabilize is approximately 3.0 ms, while the time required for the flow field of the Case 2 and Case 3 combustion chambers to stabilize is only about 2.0 ms. This may suggest that there is a direct correlation between the jet equivalence ratio and the flow field stabilization rate within a certain range. Additionally, the figure shows that the higher the global equivalence ratio of the fuel in the combustion chamber, the lower the combustion efficiency, which is actually related to the fuel mixing. In this section, the equivalence ratio is increased by arranging more injection holes. Therefore, when there are injection holes arranged upstream of the combustion chamber, continuing to arrange injection holes downstream leads to insufficient air content in the fuel mixing of the downstream injection holes, resulting in a large amount of fuel waste. To address this phenomenon, different steady flame methods of the combustion chamber have been proposed, such as adding a baffle injection in the middle of the combustion chamber. Although this also increases the global equivalence ratio of the fuel, it effectively uses the air channel in the middle of the combustion chamber, which has benefits in terms of improving the combustion efficiency. Figure 7b compares the changes of in the total pressure recovery coefficient at the outlet of the combustion chamber, varied with time, for Cases 1–3. The calculation formula is Equation (2). It was found that as the equivalence ratio increases, the total pressure recovery coefficient at the outlet generally shows an upward trend. This indicates that when the fuel equivalence ratio is higher, the intensity of the combustion shock wave string in the combustion chamber also increases, which leads to an increase in total pressure loss.

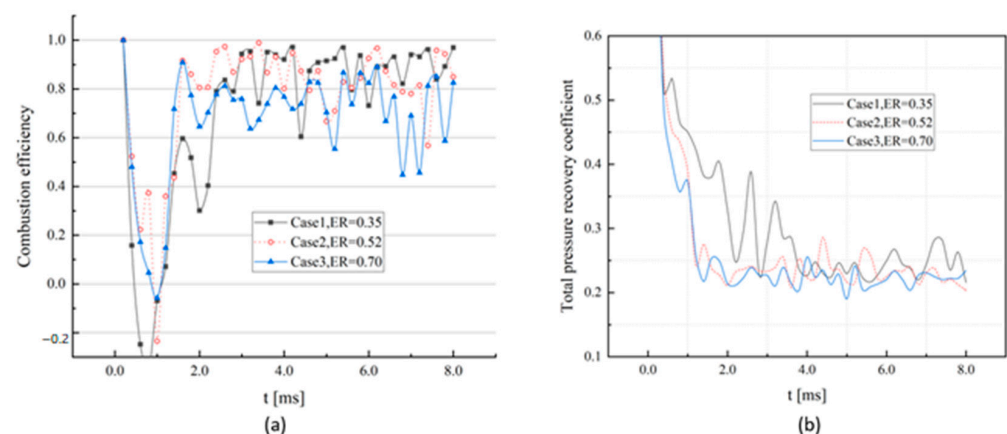


Figure 7. (a) Comparison of the averaged combustion efficiency at the outlet of the combustion chamber for Cases 1, 2, and 3; (b) Comparison of the total pressure recovery coefficient at the outlet of the combustion chamber for Cases 1, 2, and 3.

3.2. Effects of the Relative Position

The development of the mass fraction of OH free radicals in the combustion chamber of Case 4 is shown in Figure 8. Since the D1 and D3 injection holes are both arranged on

the lower wall, the combustion zone is completely located in the cavity and downstream of the cavity. At $t = 1.8$ ms, the combustion intensity is relatively low due to the initial fuel injection. With the heat release due to fuel combustion, the average pressure in the combustion chamber gradually increases, and the combustion shock wave string moves a short distance upstream. However, since the downstream nozzle is under rich combustion conditions and the combustion intensity is weaker, the overall increase in the combustion intensity of the fuel is limited. The pressure increase is relatively small, and the slight forward movement of the shock wave string almost does not change the flame stabilization mode of the combustion chamber of Case 4, i.e., the flame always remains inside the cavity or downstream of the cavity. Compared with Case 1 and Case 5, due to the weaker combustion shock wave string, the degree of boundary layer separation caused in the combustion chamber is smaller in Case 4.

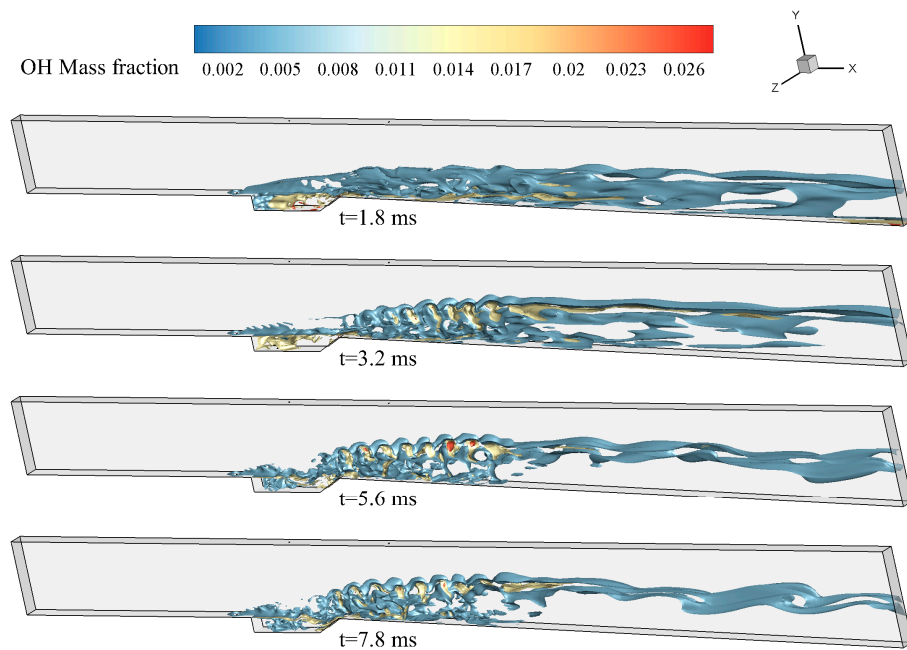


Figure 8. OH mass fraction distributions of the combustion chamber over time for Case 4.

Figure 9a shows the pressure distribution inside the combustion chamber for Cases 1–3 at $t = 8.0$ ms. It can be clearly seen that the averaged pressure in the combustion zone of Case 5 is slightly higher than that of Case 1 after the combustor flow field become stabilized. In addition, the injection in the downstream region of the Case 1 injection holes also reduces the mixing time and ignition delay of the U2 injection hole, leading to the main combustion zone on the upper wall moving in the direction of the outlet and resulting in incomplete fuel mixing and decreased combustion efficiency. Figure 9b shows the Mach number distribution inside the combustion chamber for Cases 1–3 at $t = 8.0$ ms. In the figure, it is seen that the air passage of Case 1 is close to the upper wall of the combustion chamber, while the air passage of Case 5 is symmetrically distributed around the centerline of the chamber. This indicates that the main reaction of the combustion chamber of Case 1 occurs near the cavity and the lower wall of the combustion chamber, and that the combustion intensity of U2 injection fuel is weak. However, a combustion reaction zone with similar intensity is formed near the upper and lower walls of the combustion chamber of Case 5. Because the fuel injection of Case 4 is arranged on the same side, the steady flame formation is slightly different from that of the combustion chamber in the other two cases. In Case 1 and Case 5, a single injection hole is arranged on the upper and lower walls, respectively, of the combustion chamber. The fuel from the injection holes on the upper wall is mixed and burned with the incoming air above the combustion chamber, while the fuel from the injection holes on the lower wall is mixed and burned with the incoming air below the combustion chamber. The air used between

the two injection holes, arranged on the upper wall and lower wall, respectively, does not interfere with the incoming air, so the fuel is fully mixed and burned after injection.

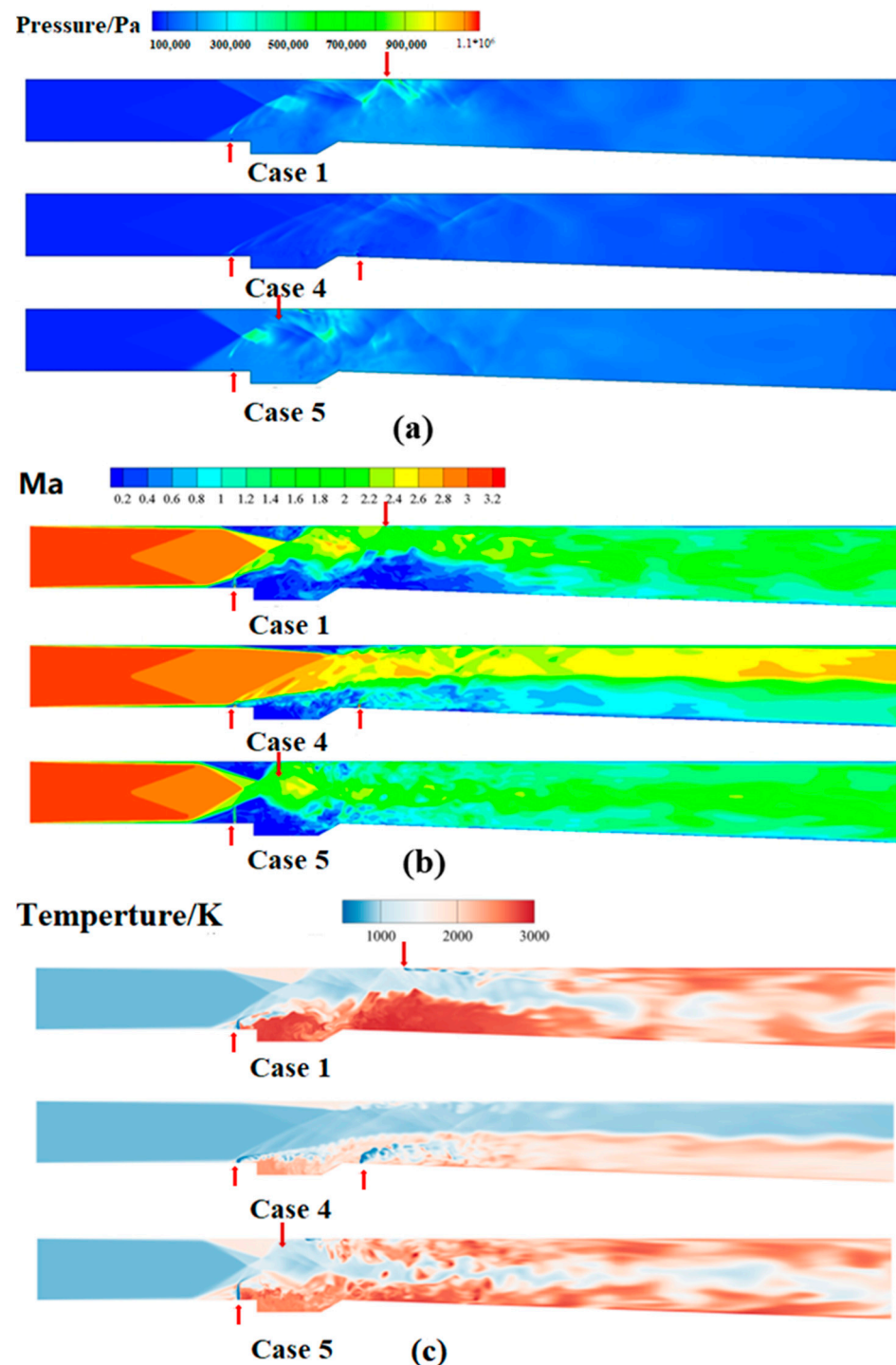


Figure 9. (a) Pressure distributions inside the combustion chamber for Cases 1, 4, and 5; (b) Mach number distribution inside the combustion chamber for Cases 1, 4, and 5. (c) Temperature distribution inside the combustion chamber for Cases 1, 4, and 5.

However, the fuel from both of the injection holes is mixed and burned with the incoming air below the combustion chamber for Case 4. When the fuel from the D1 injection hole is fully mixed and burned, the mass fraction of oxygen flowing through the D3 injection hole decreases significantly and the mass fraction of combustion thermal

products increases. Therefore, the mass fraction of oxygen around the D3 injection hole is low and the temperature is high. High temperature products have benefits for the ignition of secondary injection fuel, but a low mass fraction of oxygen is not beneficial to fuel mixing and combustion. Therefore, the combustion efficiency of the secondary injection fuel decreases significantly, and the intensity of the combustion shock string is weak. As shown in the pressure distributions of Case 4 in Figure 8, the average pressure in the combustion chamber is lower than that in the other two combustors. Compared with Case 1 and Case 5, the boundary layer separation amplitude in the combustion chamber is smaller due to the weak combustion shock string. As shown in Figure 9b, compared with the combustion mode in which the reaction zone extends from the cavity to the main stream in the other two cases, the flame of Case 4 is mainly maintained near the cavity and shear layer and barely extends to the main stream. In addition, the averaged Mach number of the air passage of Case 4 is higher than that of the other two cases, which indicates that the complex wave system formed by the interaction between the downstream bow shock wave of the combustors compresses the incoming air relatively weakly compared with the other two cases. This also confirms that the overall combustion intensity of Case 4 is relatively weak. Similar to the phenomenon described previously, a high temperature region is located in the low Mach number region, as shown in Figure 9c. The temperature distribution also indicates the combustion region where a large degree of heat release occurs.

Figure 10a compares the variations in combustion efficiency over time at the outlets of the combustion chamber for Cases 1, 4, and 5. For Case 4, where two injection holes are arranged on the same side of the wall, the reaction zone established in the combustion chamber is relatively weak, with no significant boundary layer separation, and the injection hole D3 downstream of the cavity lacks air for combustion, which results in a large amount of fuel wastage. Consequently, the combustion efficiency at the outlet in this case is the lowest. For Case 1 and Case 5, where the injection holes are arranged on the opposite sides, it can be clearly seen that the combustion efficiency at the outlet of Case 5, where the two injection holes are relatively close, is generally higher than that of Case 1 after the flow field has stabilized. This is caused by the close distance of the two injection holes, which results in a high-intensity bow shock wave upstream of the jet holes and directly causes collision interference. This promotes the mixing and combustion of the fuel that is injected into the combustion chamber, thereby increasing the combustion efficiency. In Case 1, where the two injection holes are spaced further apart, the bow shock wave has limited interference ability and cannot form a high-pressure region. Therefore, the combustion efficiency is slightly lower than in Case 5. This indicates that adopting a configuration with closely spaced injection holes on the opposite sides of the upper and lower walls can effectively increase the combustion efficiency of the fuel under supersonic multi-position injection.

A comparison of the total pressure coefficient at the outlet is shown in Figure 10b. In Case 4, where the combustion intensity is weak, the combustion chamber lacks the dissipative effect of a shock wave sequence. After the flow field stabilizes, the total pressure recovery coefficient is approximately 42%, which is significantly higher than those of the other two cases with opposite-side injection. After the flow field stabilizes in Case 1 and Case 5, the total pressure recovery coefficient at the outlet is roughly the same, i.e., around 24%. The above analysis suggests that adopting a configuration with closely spaced jet holes on opposite sides of the upper and lower walls can effectively improve the combustion efficiency and the internal pressure of the combustion chamber, even though this leads to an increase in the total pressure loss.

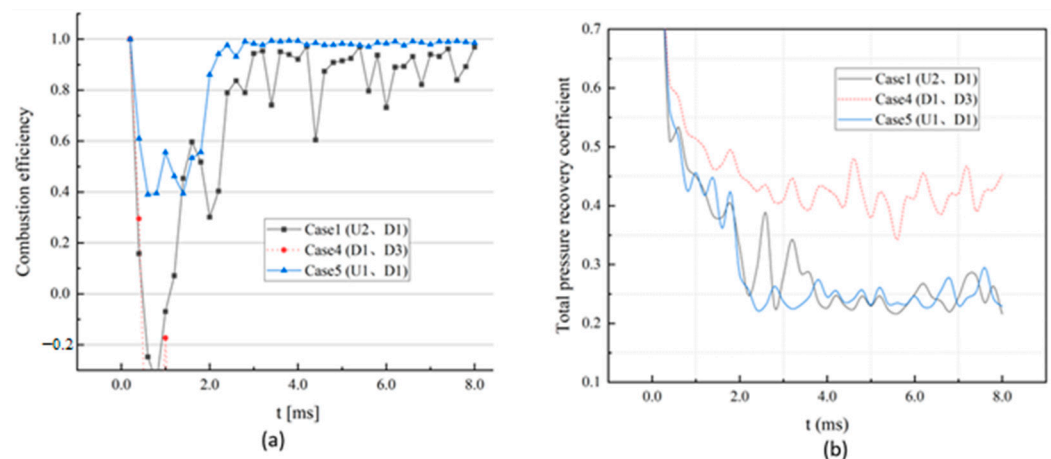


Figure 10. (a) Comparisons of the averaged combustion efficiency at the outlet of the combustion chamber varying over time for Cases 1, 4, and 5; (b) Comparisons of the total pressure recovery coefficients the outlet of the combustion chamber varying over time for Cases 1, 4, and 5.

3.3. Effect of the Injection Pressure

The effects of the injection pressure on the H_2 mass fraction and pressure distributions are displayed in Figure 11. Details of the injection pressure for Cases 1, 6, and 7 are presented. As the injection pressure increases, the depth of the hydrogen injection and the mass fraction also increase, as shown for injection hole U2 in Case 6. At the same time, a comparison of the pressure distributions reveals that as the injection pressure of the jet hole increases, the bow shock wave formed by the influence of the incoming air flow in front of the injection hole becomes stronger, and the initiation point of the shock wave is deeper. This is due to the different injection depths caused by the varied pressures, resulting in different locations of the velocity shear layer, and hence, a deeper original point for the shock wave formation. Moreover, it can be seen that the averaged pressure in the combustion chamber of Case 7 is slightly higher than those of the other two cases, at $t = 1.2$ ms. It is shown that the injection pressure on the lower wall of Case 7 is the highest, and the local equivalence ratio near the cavity is higher than in the other cases. Since the cavity plays a significant role in the mixing and ignition of the fuel, the fuel burns quickly on one side of the cavity when the equivalence ratio in the cavity region is high. The construction speed of the combustion wave system is fast, and the overall average pressure in the combustion chamber is higher at the same initial combustion time. During the initial stage of supersonic injection, the rate of pressure increase is related to the local equivalence ratio in the cavity; the higher the local equivalence ratio in the cavity, i.e., the higher the injection pressure of the injection hole on the same side upstream of the cavity, the faster the pressure in the combustion chamber increases.

The temperature and pressure distributions for Cases 1, 6, and 7 at different times ($t = 3.6$ and 7.8 ms) are shown in Figure 12. It can be observed that the combustion in Case 1 is more intense and the pressure increase is higher at $t = 3.6$ ms. The temperature and pressure distributions at different time can also indirectly show the intensity of fuel combustion and the amount of heat released. For Case 7, which has a higher injection pressure at the D1 injection hole and a larger local equivalence ratio, the average temperature at the cavity location is lower than those in Case 1 and Case 6. This indicates that fuels with a higher equivalence ratio lead to a rich combustion state within the cavity during the mid-combustion phase. The mass exchange rate between the cavity and the incoming air is low, and there is not enough air to sustain the combustion of a large amount of fuel inside the cavity. It is noted that the flow field situation in Case 1 is quite different from those in the other two cases. It has a larger high-temperature region and the average pressure in the combustion chamber is higher than the other two cases. There is also a range in the high-pressure region near the U2 injection hole. This suggests that during the mid-phase of

supersonic injection, the same pressure in the jet hole can effectively increase the combustion rate of the fuel. The combustion flow fields of the three cases are basically stable at $t = 7.8$ ms. It was found that the pressure in the combustion chambers of Case 6 and Case 7 are basically the same after stabilization, and the distribution pattern of the temperature field is also consistent. Compared with the other two cases, Case 1 has a higher average pressure in the combustion chamber, a larger high temperature region near the upper and lower walls, and a higher combustion temperature compared to the other two cases. This suggests that multi-position injection in the scramjet combustion chamber can effectively improve the combustion rate and intensity of the fuel in the scramjet combustion chamber if the global equivalence ratio of fuel injection is consistent and the injection pressure of each injection hole is maintained at close to or the same values.

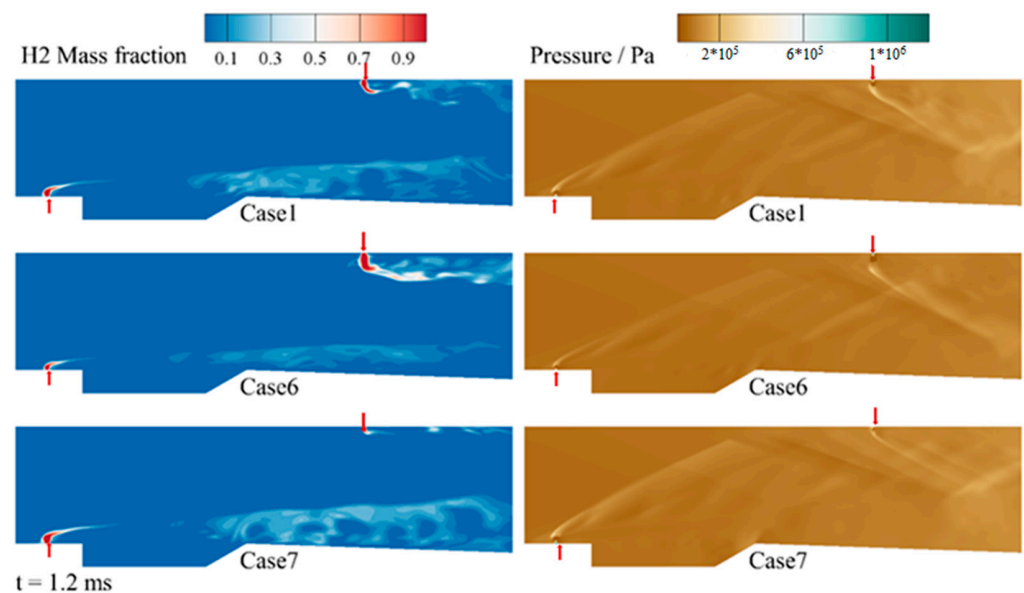


Figure 11. Comparisons of the H₂ mass fractions and pressure distributions for Cases 1, 6, and 7 at $t = 1.2$ ms.

Figure 13a shows the HO₂ radical distributions and Figure 13b the OH mass fraction distributions at $t = 8.0$ ms for Cases 1, 6, and 7. In the combustion chamber of Case 1, the HO₂ radicals produced by the combustion of fuel from the U2 and D1 injection holes collide and contact downstream in the combustion chamber. The region where HO₂ is formed nearly covers the entire spanwise cross-section, indicating that when the combustion flow field is stable, the reaction area inside the combustion chamber is large for Case 1. In contrast, it can be observed that the overall penetration depth of the HO₂ formed by the U2 injection hole for Cases 6 and 7 is lower than that in Case 1, with the reaction zone only forming near the wall. Therefore, the HO₂ radicals generated by the upper and lower walls barely make contact, and there is a relatively narrow unreacted zone between the two reaction regions for Cases 6 and 7.

Figure 14a illustrates the variations in the combustion efficiency at the outlet of the combustion chambers of Cases 1, 6, and 7. The changes in the combustion efficiency at the outlets of the combustion chambers of Case 6 and Case 7 are essentially similar, i.e., after the combustion flow field stabilizes, the combustion efficiencies at the outlets of the two combustion chambers are roughly the same. Compared to Case 1, the time required for the combustion flow field to reach a stable state is longer, i.e., about 4.5 ms. In addition, the combustion efficiency at the outlets of the two combustion chambers is approximately 70%, which is lower than that in Case 1. Figure 14b compares the changes in the total pressure recovery coefficient at the outlets of the combustion chambers of Cases 1, 6, and 7 over time. The total pressure recovery coefficients at the outlets of the combustion chambers of

Case 6 and Case 7 are essentially the same (about 27%), i.e., significantly higher than the total pressure recovery coefficient at the outlet of the combustion chamber of Case 1.

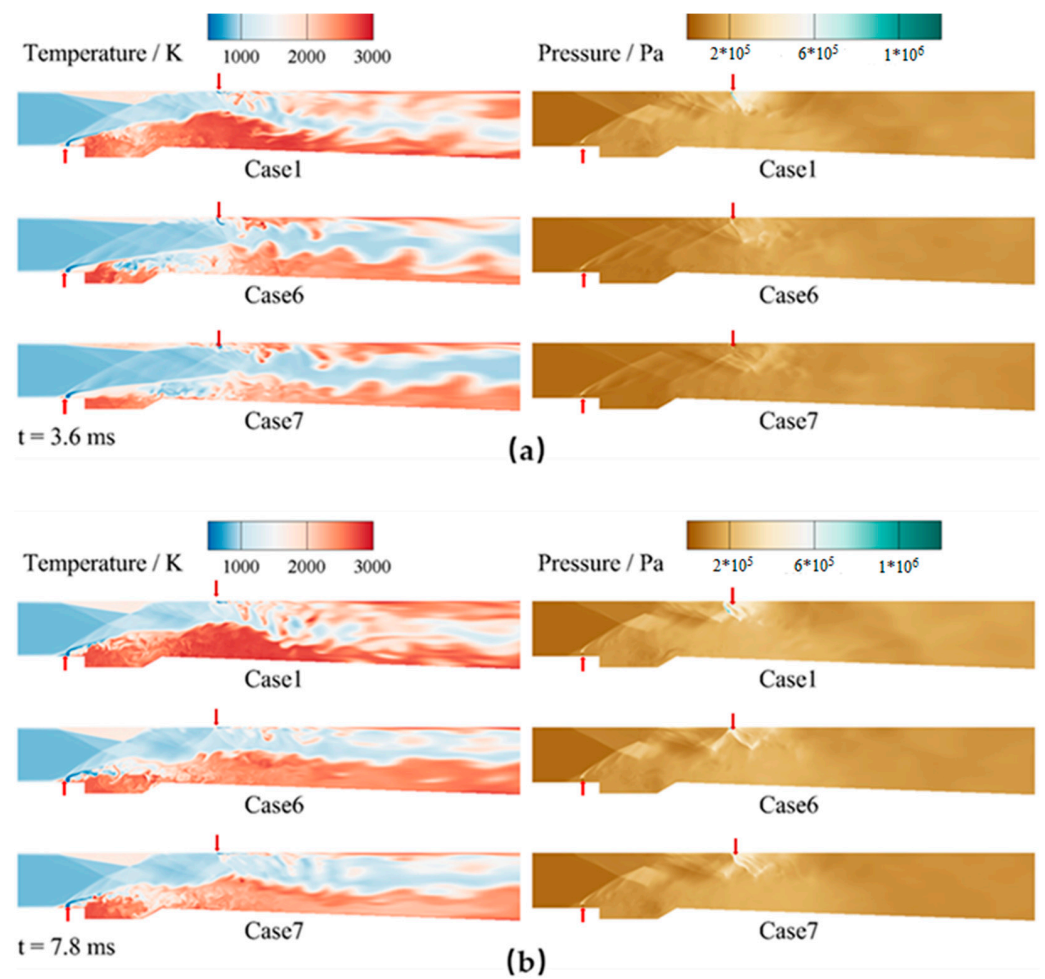


Figure 12. (a) Comparisons of the temperature and pressure distributions for Cases 1, 6, and 7 ($t = 3.6$ ms); (b) Comparisons of the temperature and pressure distributions for Cases 1, 6, and 7 ($t = 7.8$ ms).

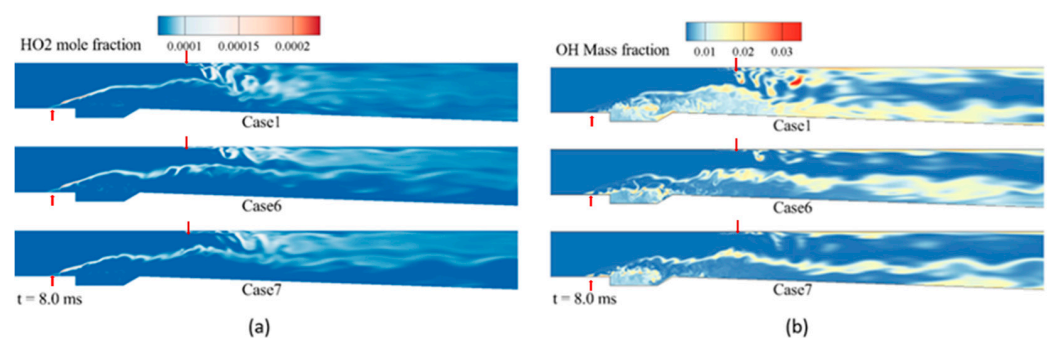


Figure 13. (a) Mole fraction distribution of HO₂ free radical for Cases 1, 6, and 7 ($t = 8.0$ ms); (b) Mass fraction distribution of HO₂ free radical for Cases 1, 6, and 7 ($t = 8.0$ ms).

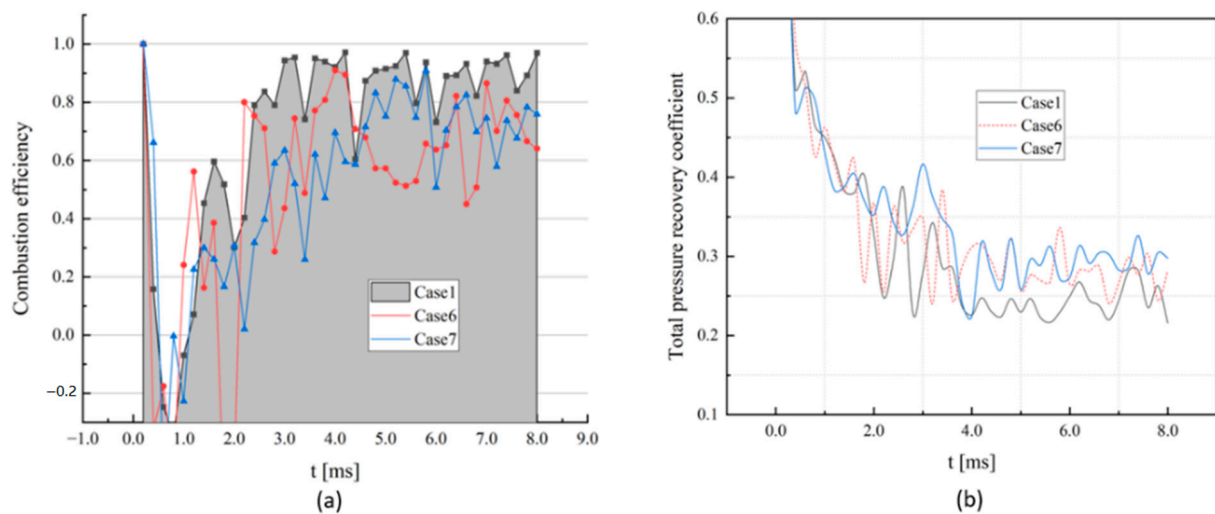


Figure 14. (a) Comparison of the combustion efficiency at the outlets of the combustion chambers over time for Cases 1, 6, and 7; (b) Comparison of the total pressure recovery coefficients at the outlets of the combustion chambers over time for Case 1, 6, and 7.

4. Conclusions

Based on the cavity stabilized flame combustion chamber of a hydrogen-fueled scramjet engine, this work adopted the one-equation LES turbulence model to define the sub-grid turbulence viscosity terms. By utilizing the finite-rate combustion model chemical reaction source and the Jachimowski 8-component, 19-step detailed reaction mechanism for hydrogen, numerical studies on the flame propagation and flow field under multi-position injection in a scramjet combustion chamber were conducted. The effects of the injection equivalence ratios, relative position, and injection pressure were analyzed.

1. With multi-position injection in a scramjet combustion chamber, the global equivalence ratio increases due to the increased number of injection holes, which leads to a higher heat release in the combustion chamber. The combustion shock wave chain advances further upstream in the combustion chamber. Moreover, the increase in the global equivalence ratio also significantly increases the average pressure in the combustion zone and the tail region of the combustion chamber when the combustion chamber flow field is essentially stable.
2. With multi-position injection in a scramjet combustion chamber, adopting closely spaced injection points, arranged on the opposing sides of the upper and lower walls, can effectively improve the combustion efficiency of the fuel and the internal pressure of the combustion chamber; however, this also causes an increase in the total pressure loss. When the injection holes are arranged on the same side of the wall, the fuel ejected from multiple injection holes mixes and burns with the incoming air on one side of the combustion chamber. After the fuel ejected from the upstream injection ports has been fully mixed and burned, the oxygen mass fraction of the flow passing through the downstream injection hole significantly decreases. The combustion heat product increases and the mass fraction of oxygen around the fuel is lower. This is beneficial for the ignition of secondary fuel injection but not beneficial for fuel mixing and burning, leading to a significant drop in the combustion efficiency from the secondary injection holes and a decrease in the intensity of the combustion shock wave chain.
3. Multi-position injection in a scramjet combustion chamber can effectively increase the stability speed of the combustion chamber flow field and the overall combustion efficiency if the global equivalence ratio of the fuel injection is consistent and the injection pressure of the injection holes is maintained at close to or the same values. In addition, it causes the reaction zone to move backwards and leads to an increase

in the pressure at the tail of the combustion chamber if the injected fuel is located downstream and the injection pressure is higher.

4. With multi-position injection in a scramjet combustion chamber, the pressure increase rate inside the combustion chamber during the initial stage of scramjet injection is related to the local equivalence ratio of the cavity. In other words, the higher the local equivalence ratio of the cavity, i.e., the higher the injection pressure of the injection holes arranged upstream and on the same side of the cavity, the faster the pressure increase in the combustion chamber.

Author Contributions: Methodology, W.X. and J.L.; Software, T.D. and Z.L.; Investigation, H.X.; Original draft preparation, W.X. and H.X.; Review and editing, T.D., Z.L. and J.L. All authors have read and agreed to the published version of the manuscript.

Funding: This work was supported by Key Laboratory Continuously Supporting Project (grant No. WDZC6142703202216), the Natural Science Foundation of Hunan Province (Grant No. 2023JJ40733) and the National Natural Science Foundation of China (Grant No. 12272133).

Data Availability Statement: For privacy reasons, we cannot share research data.

Conflicts of Interest: The authors declare no conflict of interest.

Nomenclature

Latin characters

L	Combustion chamber length (mm)
ΔL	Distance between the entrance and the cavity (mm)
l	Total cavity length (mm)
H	Entrance height (mm)
h	Concave cavity height (mm)
W	Computational domain width (mm)

Greek symbols

γ	Inclination angle of the back wall of the cavity (°)
ϕ	Oxygen consumption rate
σ	Total pressure recovery factor
ϕ	Combustion efficiency
θ	Expanded angle of the combustion chamber (°)

Subscripts

0	Total
t	Gas injection
m	Mass

Abbreviations

ER	Equivalent ratios
PLIF	Planar Laser-Induced Fluorescence
Ma	Mach number
ms	Millisecond

References

1. Roudakov, A.S.; Schikhman, Y.; Semenov, V. Flight Testing an Axisymmetric Scramjet-Russian Resent Advances. In Proceedings of the 44th IAF Congress, Graz, Austria, 16–22 October 1993; p. S.4.485.
2. Vinogradov, V.A.; Kobigsky, S.A.; Petrov, M.D. Experimental investigation of kerosene fuel combustion in supersonic flow. *J. Propuls. Power* **1995**, *11*, 130–134. [[CrossRef](#)]
3. Owens, M.G.; Tehranian, S.; Segal, C.; Vinogradov, V.A. Flame-holding configurations for kerosene combustion in a Mach 1.8 airflow. *J. Propuls. Power* **1998**, *14*, 456–461. [[CrossRef](#)]
4. Ortwerth, P.; Mathur, A.; Vinogradov, V.; Grin, V.; Goldfeld, M.; Starov, A. Experimental and numerical investigation of hydrogen and ethylene combustion in a Mach 3-5 channel with a single injector. In Proceedings of the 32nd Joint Propulsion Conference and Exhibit, Lake Buena Vista, FL, USA, 1–3 July 1996; p. 3245.
5. Ben-Yakar, A.; Kamel, M.; Morris, C.; Hanson, R.; Ben-Yakar, A.; Kamel, M.; Morris, C.; Hanson, R. Experimental investigation of H2 transverse jet combustion in hypervelocity flows. In Proceedings of the 33rd Joint Propulsion Conference and Exhibit, Seattle, WA, USA, 6–9 July 1997; p. 3019.

6. Lee, J.H.; Lee, E.S.; Han, H.S.; Kim, M.S.; Choi, J.Y. A Study on a Vitiated Air Heater for a Direct-Connect Scramjet Combustor and Preliminary Test on the Scramjet Combustor Ignition. *Aerospace* **2023**, *10*, 415. [\[CrossRef\]](#)
7. Meng, Y.; Sun, W.; Gu, H.; Chen, F.; Zhou, R. Supersonic Combustion Mode Analysis of a Cavity Based Scramjet. *Aerospace* **2022**, *9*, 826. [\[CrossRef\]](#)
8. Penzin, V. *Experimental Investigation of Supersonic Flows with Separated Regions in Ducts*; Central Aerodynamic Institute Moscow: Moscow, Russia, 1995.
9. Le, D.B. Scramjet Isolator Flow Studies. In Proceedings of the 2005 Virginia Space Grant Consortium Student Research Conference, Newport News, VA, USA, 1 April 2005.
10. Lin, K.C.; Tam, C.J.; Jackson, K.; Kennedy, P.; Behdadnia, R. Experimental investigations on simple variable geometry for improving scramjet isolator performance. In Proceedings of the 43rd AIAA/ASME/SAE/ASEE Joint Propulsion Conference & Exhibit, Cincinnati, OH, USA, 8–11 July 2007; p. 5378.
11. Tam, C.J.; Eklund, D.; Behdadnia, R. Influence of downstream boundary conditions on scramjet-isolator simulations. In Proceedings of the 26th AIAA Applied Aerodynamics Conference, Honolulu, HI, USA, 18–21 August 2008; p. 6929.
12. Chang, J.; Fan, Y.; Bao, W.; Yu, D.; Shen, Y. Unstart margin control of hypersonic inlets. *Acta Astronaut.* **2010**, *66*, 78–87. [\[CrossRef\]](#)
13. Lin, K.C.; Tam, C.J.; Jackson, K.; Eklund, D.; Jackson, T. Characterization of shock train structures inside constant-area isolators of model scramjet combustors. In Proceedings of the 44th AIAA Aerospace Sciences Meeting and Exhibit, Reno, NV, USA, 9–12 January 2006; p. 816.
14. Ben-Yakar, A.; Hanson, R. Supersonic combustion of cross-flow jets and the influence of cavity flame-holders. In Proceedings of the 37th Aerospace Sciences Meeting and Exhibit, Reno, NV, USA, 11–14 January 1999; p. 484.
15. Johansen, C.T.; McRae, C.D.; Danehy, P.M.; Gallo, E.C.; Cantu, L.M.; Magnotti, G.; Cutler, A.D.; Rockwell, R.D.; Goyne, C.P.; McDaniel, J.C. OH PLIF visualization of the UVa supersonic combustion experiment: Configuration A. *J. Vis.* **2014**, *17*, 131–141. [\[CrossRef\]](#)
16. Carter, C.D.; Hammack, S.; Lee, T. High-speed flamefront imaging in premixed turbulent flames using planar laser-induced fluorescence of the CH C–X band. *Combust. Flame* **2016**, *168*, 66–74. [\[CrossRef\]](#)
17. Cantu, L.M.; Gallo, E.C.; Cutler, A.D.; Danehy, P.M.; Rockwell, R.D.; Johansen, C.T.; Goyne, C.P.; McDaniel, J.C. OH PLIF visualization of a premixed ethylene-fueled dual-mode scramjet combustor. In Proceedings of the 54th AIAA Aerospace Sciences Meeting, San Diego, CA, USA, 4–8 January 2016; p. 1763.
18. Moura, A.F.; Gibbons, N.; Wheatley, V.; McIntyre, T.; Jahn, I. Characterization of supersonic turbulent combustion in a mach-10 scramjet combustor. *AIAA J.* **2020**, *58*, 2180–2196. [\[CrossRef\]](#)
19. Cao, R.; Chang, J.; Bao, W.; Guo, M.; Qin, J.; Yu, D.; Wang, Z. Analysis of combustion mode and operating route for hydrogen fueled scramjet engine. *Int. J. Hydrog. Energy* **2013**, *38*, 5928–5935. [\[CrossRef\]](#)
20. Choubey, G.; Yuvarajan, D.; Huang, W.; Yan, L.; Babazadeh, H.; Pandey, K.M. Hydrogen fuel in scramjet engines—A brief review. *Int. J. Hydrog. Energy* **2020**, *45*, 16799–16815. [\[CrossRef\]](#)
21. Choubey, G.; Devarajan, Y.; Huang, W.; Mehar, K.; Tiwari, M.; Pandey, K.M. Recent advances in cavity-based scramjet engine—a brief review. *Int. J. Hydrog. Energy* **2019**, *44*, 13895–13909. [\[CrossRef\]](#)
22. Kannaiyan, K. Numerical investigation of the local and global supersonic combustion characteristics of ethylene fuel. *Aerosp. Sci. Technol.* **2020**, *106*, 106178. [\[CrossRef\]](#)
23. He, Z.; Wang, H.; Li, F.; Tian, Y.; Wan, M.; Zhu, J. Effect of Fuel-Injection Distance and Cavity Rear-Wall Height on the Flameholding Characteristics in a Mach 2.52 Supersonic Flow. *Aerospace* **2022**, *9*, 566. [\[CrossRef\]](#)
24. Ma, S.; Zhong, F.; Zhang, X. Numerical study on supersonic combustion of hydrogen and its mixture with Ethylene and methane with strut injection. *Int. J. Hydrog. Energy* **2018**, *43*, 7591–7599. [\[CrossRef\]](#)
25. Liu, Y.; Tan, J.; Wan, M.; Zhang, L.; Yao, X. Quantitative measurement of OH* and CH* chemiluminescence in jet diffusion flames. *ACS Omega* **2020**, *5*, 15922–15930. [\[CrossRef\]](#)
26. Xi, W.; Xu, M.; Liu, C.; Liu, J.; Sundén, B. Generation and Propagation Characteristics of an Auto-Ignition Flame Kernel Caused by the Oblique Shock in a Supersonic Flow Regime. *Energies* **2022**, *15*, 3356. [\[CrossRef\]](#)
27. Wang, H.; Wang, Z.; Sun, M. Experimental study of oscillations in a scramjet combustor with cavity flameholders. *Exp. Therm. Fluid Sci.* **2013**, *45*, 259–263. [\[CrossRef\]](#)
28. Horiuti, K. Large eddy simulation of turbulent channel flow by one-equation modeling. *J. Phys. Soc. Jpn.* **1985**, *54*, 2855–2865. [\[CrossRef\]](#)
29. Jachimowski, C.J. *An Analytical Study of the Hydrogen-Air Reaction Mechanism with Application to Scramjet Combustion*; NASA: Washington, DC, USA, 1988.
30. Mitani, T.; Kouchi, T. Flame structures and combustion efficiency computed for a Mach 6 scramjet engine. *Combust. Flame* **2005**, *142*, 187–196. [\[CrossRef\]](#)
31. Génin, F.; Menon, S. Simulation of turbulent mixing behind a strut injector in supersonic flow. *AIAA J.* **2010**, *48*, 526–539. [\[CrossRef\]](#)

Disclaimer/Publisher’s Note: The statements, opinions and data contained in all publications are solely those of the individual author(s) and contributor(s) and not of MDPI and/or the editor(s). MDPI and/or the editor(s) disclaim responsibility for any injury to people or property resulting from any ideas, methods, instructions or products referred to in the content.